Lightweight Triboelectric Nanogenerators Based on Hollow Stellate Cellulose Films Derived from Juncus effusus L. Aerenchyma

Chen, Qi; Li, Wenjian; Yan, Feng; Maniar, Dina; van Dijken, Jur; Rudolf, Petra; Pei, Yutao; Loos, Katja

Published in:
Advanced Functional Materials

DOI:
10.1002/adfm.202304801

ADVANCED FUNCTIONAL MATERIALS
www.afm-journal.de

Lightweight Triboelectric Nanogenerators Based on Hollow Stellate Cellulose Films Derived from *Juncus effusus* L. Aerenchyma

*Qi Chen, Wenjian Li, Feng Yan, Dina Maniar, Jur van Dijken, Petra Rudolf, Yutao Pei, and Katja Loos**

This study reports a facile delignification and natural drying process for synthesizing cellulose films using the unique surface roughness, porosity, and lightness of the hollow stellate cellulose (HSC) united aerenchyma of the wetland weed *Juncus effusus* L. By controlling the grafted amino/fluorine-bearing group content of various silane coupling agents, this work successfully manipulates the triboelectric polarities of HSC films after silanization. Subsequently, a layer of Ag nanowire electrodes is coated on one side of the silanized HSC friction layers, resulting in flexible, lightweight, semi-transparent HSC-based triboelectric nanogenerators (HSC-TENGs) featuring both macro-scale surface roughness and micro-nano inner pores. These all-in-one HSC-TENGs achieve the highest output voltage of 4.86 V, which is 28 times that of TENGs employing two pristine HSC films as triboelectric layers (PHSC-TENG). Finally, the HSC-TENG with the optimum output power is applied as a wearable self-powered sensor for gait analysis, demonstrating stable and sustainable performances in distinguishing different body motions such as walking, running, jumping, and calf raising. This study not only proposes a new cellulose-based TENG for future in-depth body locomotion analysis but also paves the way for converting differently structured aerenchyma from abundant problematic aquatic or wetland weeds into promising structural templates in multifunctional cellulose-based applications.

1. Introduction

In recent decades, the miniaturization of flexible and wearable devices has led to an increase in electronic waste and environmental pollution from the periodic replacement of their batteries.[1–6] The traditional power supply's bulky size and weight have become a barrier to further electronics miniaturization, physical burden reduction, and cost economization.[7,8] Triboelectric nanogenerators (TENG), discovered as a novel micron nanoenergy harvester, have gained increasing attention due to their ability to convert small amounts of wasted mechanical energy into nanoscale electrical energy.[9] The working principle of a TENG is based on the triboelectric effect and the electrostatic induction between two contacting layers with dissimilar tribopolarities. There is a wide selection of friction materials known as the triboelectric series.[10] Although many materials have been studied or used as friction parts,[7,11–20] the replacement of petroleum-based, non-recyclable organic friction materials with renewable, natural materials that are fully

Q. Chen, D. Maniar, J. van Dijken, K. Loos
Macromolecular Chemistry and New Polymeric Materials
Zernike Institute for Advanced Materials
University of Groningen
Nijenborgh 4, Groningen 9747 AG, The Netherlands
E-mail: k.u.loos@rug.nl

W. Li, Y. Pei
Advanced Production Engineering, Engineering and Technology Institute Groningen
University of Groningen
Nijenborgh 4, Groningen 9747 AG, The Netherlands

F. Yan, P. Rudolf
Surfaces and Thin Films, Zernike Institute for Advanced Materials
University of Groningen
9747 AG, Nijenborgh 4 Groningen, The Netherlands

The ORCID identification number(s) for the author(s) of this article can be found under https://doi.org/10.1002/adfm.202304801

DOI: 10.1002/adfm.202304801

biocompatible, biodegradable, or recyclable is still crucial in the current energy crisis and environmental pollution situation.[21,22]

Cellulose-based triboelectric nanogenerators have had the most significant achievements among reported biomass-derived nanogenerators. This is due to the outstanding advantages of cellulose, which include widespread availability, renewability, biodegradability, biocompatibility, low cost, versatility, and frictional electrical activity.[1,23] Additionally, the numerous hydroxyl groups of cellulose provide strong hydrogen bonds and chemical reactive sites for chemical modifications,[24] which can improve the material's strength and optimize its electrical performance in TENGs. However, the natural drawbacks of cellulose, including poor solubility and processability, can also be significant obstacles in TENG applications. To overcome these challenges, two main approaches have been proposed in the literatures. The first approach involves the extraction of natural cellulose into cellulose nanofibers,[25] or cellulose nanocrystals via mechanical methods (e.g., ultrasonic crushing, mechanical stirring, high-pressure homogenization),[26] chemical methods (2,2,6,6-tetramethylpiperidine-1-oxyl radical-mediate oxidation,[27] acid hydrolysis),[28] or biological methods (bacterial secretion, i.e., bacterial cellulose).[8] The second approach involves natural cellulose that can be regenerated via recrystallization and precipitation immediately after dissolving it in various solvents, such as ionic liquids,[29] N-methylmorpholine-N-oxide,[30] N,N-dimethylacetamide/LiCl systems,[30] and alkali/urea aqueous solutions.[31,32]

After successfully obtaining processable cellulose fibers, the subsequent formation of cellulose films is also essential for increasing TENG output and reducing weight by improving film roughness and porosity, respectively. As reported earlier, various additional methods have been carried out for these two purposes, including plasma etching,[33] 3D printing,[34] freeze drying,[35] electrospinning,[26,36] and micro/nano patterning.[37] However, this means that significant effort, energy, and chemicals are required for processing raw natural cellulose into favorable cellulose-based triboelectric layers, which is contrary to the original intention of designing cellulose-based TENGs for energy savings and environmental protection. Therefore, there is an urgent need for simpler, more efficient, and more environmentally friendly methods of treating natural cellulose to advance the development of cellulose-based TENGs.

Juncus effusus L. (JE) is a wetland perennial monocot that is widely distributed as one of the dominant species throughout warm temperature zones within multiple altitude ranges.[38] Due to its high seed production, *Juncus effusus* L. was assessed as a problematic weed in pastures and meadows because it impairs forage yield and quality.[39,40] Moreover, it has a relatively large annual production of ≈10 kg ash-free dry mass per square meter,[41] which costs millions of dollars annually to control its quantities.[40,42] Thus, reasonable and valuable applications for this prolific pest are of high interest. The epidermis of the JE stem was usually utilized in weave, while its pith was historically applied as wicks in train-oil lamps across northwestern Europe and China due to the highly porous structures, which were provided by the plant tissue – aerenchyma.[43] Aerenchyma contains different characteristic patterns arrangement (radial,[44] perpendicular, honeycomb,[36] or stellate)[45] with large intercellular spaces. This spongy plant tissue commonly exists in aquatic and wetland species, assisting their floating and internal air circulation functions. Recently, characterized by a unique 3D stellate network,[118] this cellulosic aerenchyma foam of *Juncus effusus* L. was also found to be applicable in solar-driven steam generators and soluble pollutant removal.[46] Nevertheless, the application of *Juncus effusus* L. aerenchyma foams in TENG applications has not yet been reported.

In this study, we propose a hollow stellate cellulose-based TENG (HSC-TENG) with surface modifications and Ag nanowire electrodes deposition. The hollow stellate cellulose (HSC) films were fabricated with unique hollow stellate cellulose fibers from the aerenchyma of *Juncus effusus* L., which shows the enhanced surface roughness, porosity, and lightness. The triboelectric polarities of HSC films were successfully enhanced and tuned by controlling the contents of grafted amino/fluorine-bearing groups from various silane coupling agents. As a result, the highest HSC-TENGs' output was improved to 4.86 V with silanized HSC friction layers. This output was 28 times that of TENGs employing two pristine HSC films as triboelectric layers (PHSC-TENG). This material was subsequently applied as a wearable self-powered sensor with stable and long-term output performance for distinguishing different body motion states, such as walking, running, jumping and calf raising. Hence, the proposed HSC-TENG here demonstrates a high potential as a promising material for detailed analysis of body locomotion. Additionally, the findings reported in this study provide new insights into the utilization of differently structured aerenchyma from abundant problematic aquatic or wetland weeds as potential structural templates for multifunctional cellulose-based applications.

2. Results and Discussion

The procedure to obtain pristine hollow stellate cellulose (PHSC) and to fabricate hollow stellate cellulose-based TENG (HSC-TENG) is shown in **Figure 1**e, and the corresponding detailed methods could be found in the supporting information. Briefly, PHSC film was first synthesized by delignifying,[47] dialyzing, and naturally drying the *Juncus effusus* L. aerenchyma (JEA) samples collected from nature (Figure 1a,b). The obtained PHSC film was found semitransparent, bendable and lightweight as shown in Figure 1h,i. Then, PHSC film were aminated as the positive friction layer N_xHSC (x = 1, 3) and fluorinated as the negative friction layer F_yHSC (y = 13, 21) using (3-aminopropyl)triethoxysilane/3-[2-(2-aminoethylamino)ethylamino]propyl-trimethoxysilane (APTES/DETAS) and trichloro(1H,1H,2H,2H-perfluorooctyl)silane/1H,1H,2H,2H-perfluorododecyltrichlorosilane (FOTS/FTCS), respectively, to realize the HSC-TENGs. The amino groups in N_xHSC could enhance the electrons donating ability on their surface, while the fluoro groups in F_yHSC tends to draw electrons during contact electrification. Additionally, lightweight Ag nanowires were used as backside electrodes (Figure 1f) of the all-in-one HSC-TENG. As a result, N_xHSC and F_yHSC can act as the triboelectric layers, inductive electrode and substrate at the same time. This design not only improved the output performance of the cellulose-based HSC-TENG TENG, but also ensured its overall sustainability by utilizing widely reported biodegradable silanized cellulose materials.[48-52] The

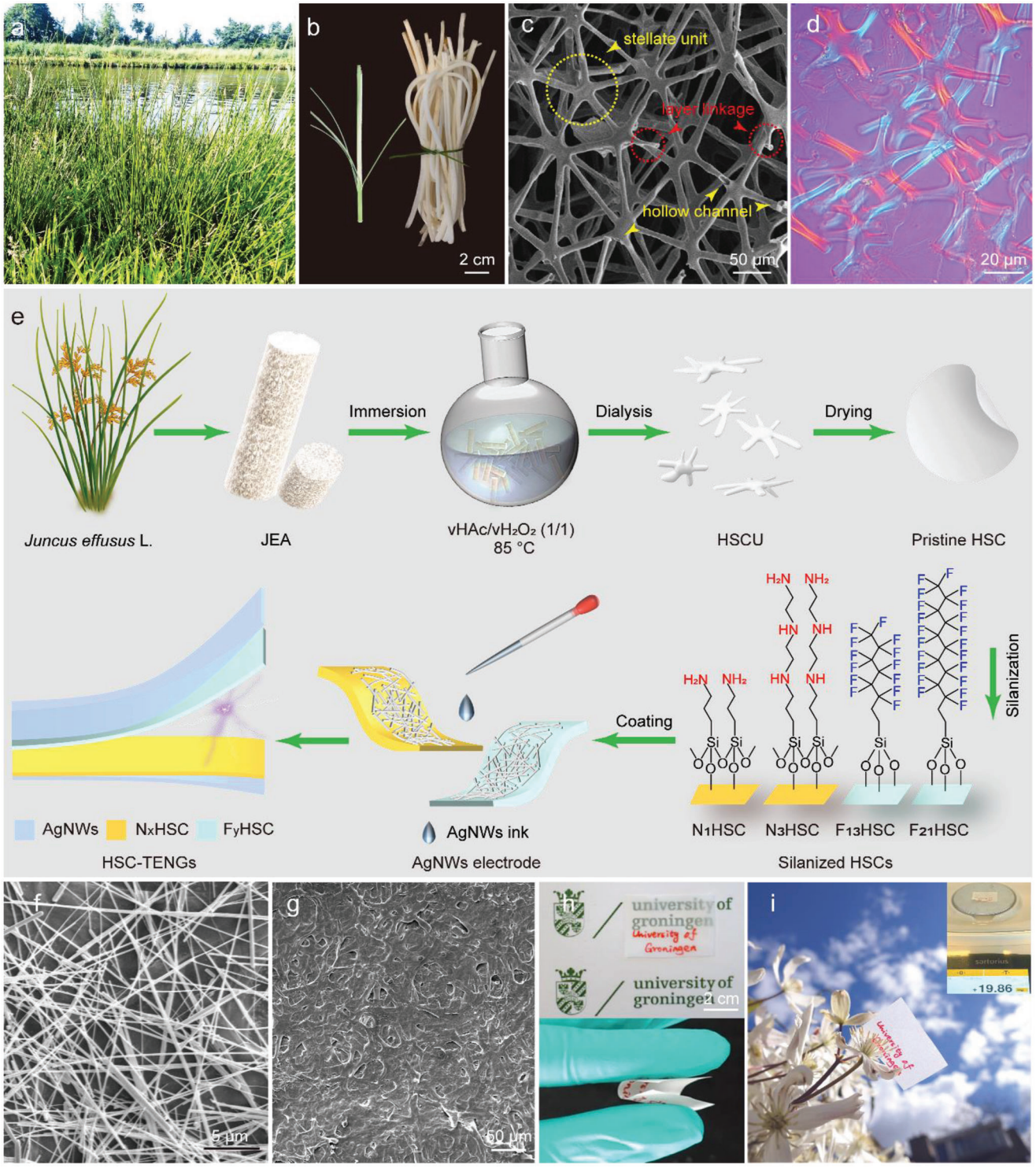

Figure 1. a) *Juncus effusus* L. (JE) b) Extracted JE aerenchyma (JEA) foams. c) SEM image of the JEA network. d) Polarized optical microscopy image of the hollow stellate cellulose units (HSCU). e) Schematic of the HSC-TENG preparation process and structures. f) SEM image of the AgNWs electrode. g) SEM image of the pristine hollow stellate cellulose (PHSC) film surface. h) Semitransparent and bendable PHSC. i) Lightweight PHSC (3 cm × 2 cm, 19.86 mg).

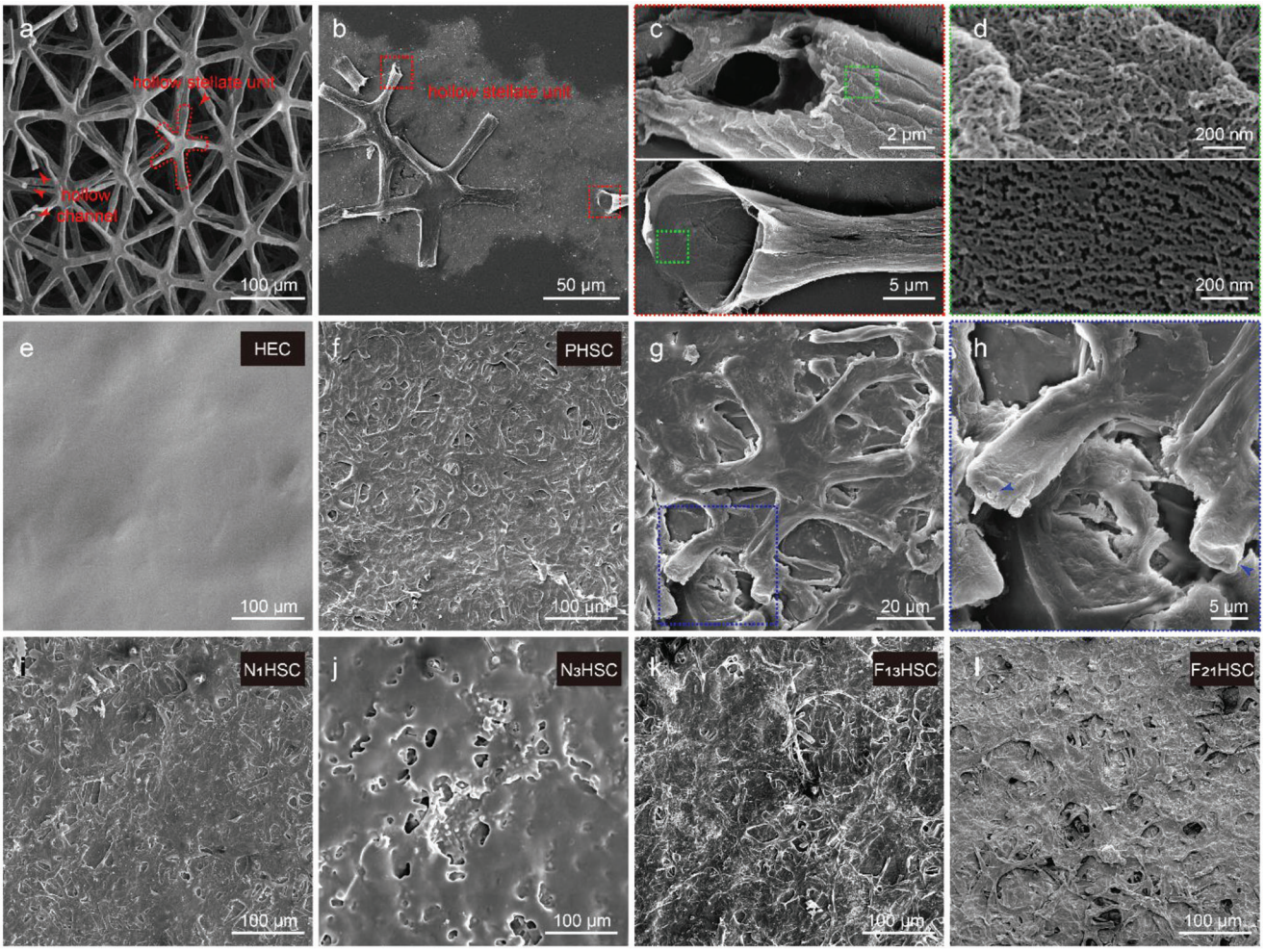

Figure 2. SEM images of a) JEA network, b) HSCU, c) zoomed-in red boxed areas, d) zoomed-in green boxed areas, e) HEC, f) PHSC, g) HSCU within fabricated PHSC film, h) enlarged blue boxed area, i) N_1HSC, j) N_3HSC, k) F_{13}HSC, and l) F_{21}HSC, respectively.

morphologies of the samples at each step were observed with scanning electron microscopy (SEM), as shown in **Figure 2**.

To separate hollow stellate cellulose units (HSCU) from *Juncus effusus* L. samples, a facile delignification method was used.[47] *Juncus effusus* L., as the aerenchyma tissue, contains well-developed interconnected air chambers that ensure the plant's continuous oxygen supply and buoyancy support within the wetland environment.[44] These symmetrical and regular air channels are shaped by the multicellular lignocellulosic walls along both transverse and longitudinal directions, which also results in the snow-like whiteness of JEA. The stellate lignocellulosic microtubes are considered structural units that are regularly interconnected to assemble the 3D JEA structure (Figure 2a). The bulged linkages of these stellate units, consisting of lignin and hemicellulose, were removed after the delignification process, while the cellulosic HSCU remained. HSCU cylinder walls became less stiff and tend to overlap after delignification (Figure 2b) due to the removal of lignin molecules that strengthen the cell wall through cross-linking of plant polysaccharides and cellulose.[53] SEM characterization shows a rough surface with nanopores on both the inner and outer walls of the isolated HSCU (Figure 2c,d). This crystallized rough-surfaced cellulose HSCU (Figure 1d) with a unique hollow stellate shape was then collected for further preparation of HSC film.

After settling at the bottom of the Teflon mold, the wet HSCUs aggregated and consolidated due to the strong plasticizing effect of water.[54] Upon delignification, HSCUs can become highly hydrated and efficiently packed in water due to their small size and capillary pressure. As more water evaporates during the drying process, the wet HSCUs are drawn closer together due to increased capillary pressure caused by the reduced radius of the capillaries.[55] Finally, fiber-fiber joints among HSCUs were generated by cellulose hydrogen bonds at direct contact points of the fibers.

It is noteworthy that the HSCUs have a relatively rougher surface compared to the smooth elementary cellulose fibril, resulting in the significant surface roughness difference between the hydroxyethyl-cellulose (HEC) film and PHSC film (Figure 2e,f). The rough surface of HSCUs indicates that not all HSCU interfaces realized molecular contacts while drying, whereas other separated parts shaped the inner cavities (Figure 2g) for a porous structure. The HSCU itself tends to form a dumbbell-like or flat

configuration with minimal space inside (Figure 2h), determined by the balance between the rigidity of the tube walls and the H—bond/van der Waals force.[55,56]

Instead of using reported methods such as freeze drying, electrospinning, or micro/nanopatterning to boost the porosity and surface area of cellulose–based triboelectric films,[26-35] delignified HSCUs contribute directly to the surface roughness and micro-nano porous structure of PHSC films. Fabrication of PHSC films is completed by a simple natural drying process, without the need for mechanical compression.[26,35] This biomass-derived cellulose-based film exhibits a rough surface and inner porous structure, while also demonstrating noteworthy characteristics such as lightness (grammage: 27.9 ± 0.4 g m^{-2}), thinness (thickness: 33.2 ± 2.6 µm), and low density (843.5 ± 55.3 kg m^{-3}). These characteristics are comparable or improved to various cellulose nanopapers (Table S1, Supporting information), while utilizing more facile, cost-effective, and environmentally friendly manufacturing processes compared with other alternative cellulose nanopaper synthesis methods. In addition, PHSC film also exhibited a bendable characteristic as shown in Figure 1h. In order to further evaluate the mechanical reliability of PHSC film, its tensile strength was tested before and after subjecting it to 5000 continuous bending cycles (Figure S1, Supporting information). The tensile strength of PHSC was measured to be 46.8 MPa and showed a slight decrease to 40.0 MPa after the 5000 bending cycles. This proves that the PHSC film sustains a relatively stable mechanical strength after continuously repeated bending. Notably, the tensile strength of the PHSC was significantly higher than that of cellulose nanopaper (203 kPa) derived from a similar biomass source (Canola straw).[57] This higher tensile strength can be attributed to the larger contacting/bonding surface of cellulose fibers as well as hemicellulose residues resulting from the delignified macro-sized HSCU.[58,59] However, it is also noteworthy that the reported tensile strength of bacterial cellulose nanopaper (100 MPa) and wood-based nanofibrillated cellulose nanopaper (150 MPa) was approximately two and three times that of PHSC.[59] This lower tensile strength can be explained by the unique porous structure of HSCU in PHSC, as reduced tensile strength results can be commonly found in materials with larger porosity.[60,61] In summary, the synthesized PHSC offered a facile and environmentally friendly method to obtain the cellulose-based friction layer that exhibits roughness, porosity, lightweight and flexibility at the same time. These characteristics and unique structures of PHSC also enabled its potentials for further optimizations in TENG applications.

On the basis of their superior morphology and structure, PHSC films were further aminated as a positive friction layer (N_xHSC) or fluorinated as a negative friction layer (F_yHSC) to realize various hollow stellate cellulose-based TENGs (HSC-TENGs) without petroleum-based, nonrecyclable organic friction materials. As shown schematically in Figure 1e, four silane coupling agents containing amino and fluorine-rich groups, namely, APTES, DETAS, FOTS, and FTCS were utilized here and the corresponding modified films were named N_1HSC, N_3HSC, F_{13}HSC, and F_{21}HSC, respectively. Subsequently, the modifications of these obtained N_xHSC and F_yHSC films were verified with fourier-transform infrared spectroscopy (FTIR), X-ray diffraction (XRD), water contact angle measurement (WCA), and X-ray photoelectron spectroscopy (XPS) characterization, as shown in **Figure 3**.

The silanization of PHSC films was evaluated with FTIR. Four regions of the spectra with obvious absorption peak differences are magnified at ≈3600–3000, ≈1590–1510, ≈1260–1120, and ≈1010–750 cm^{-1} (see Figure 3a). It is important to note that the observed peak centers of natural materials could vary by ≈±16 cm^{-1} among different studies.[62] The clear broad peak at 3331 cm^{-1} represents the hydroxyl and carboxylic O—H stretching vibrations in cellulose I,[63–66] indicating either the oxygen-rich groups or unreacted hydroxyl groups within the PHSC films before and after surface modifications. As these oxygen-rich groups with lone electrons were reported to have strong electron donating ability,[26] the positive triboelectric tendency of the friction materials could be accordingly enhanced. The positive polarity of PHSC films was further enhanced by grafting with amino groups, which could be confirmed by the new appearance of absorption peaks attributed to N_1HSC and N_3HSC at 1576 cm^{-1} (N—H bending vibration of primary amino groups)[67] and 1543 cm^{-1} (N—H bending vibration of secondary amine groups),[67] respectively. Another typical N—H stretching vibration peak in the region of ≈3336–3282 cm^{-1} overlapped with the broad peak of the O—H stretching vibrations and cannot be observed here.[68] For the negative friction materials F_{13}HSC and F_{21}HSC, two newly appeared absorption bands were found at 1203 and 1149 cm^{-1}, which corresponds to the stretching vibrations of —CF_2 and —CF_3, respectively.[69,70] A peak at 1057 cm^{-1}, which corresponded to Si—O—Si group stretching, Si—O—C asymmetrical stretching, or C—O—C symmetric stretching in cellulose, was observed in both the N_xHSC and F_yHSC spectra.[71,72] Thus, this peak together with the absorbance peak appearance at 810 cm^{-1} (Si—O—C group symmetric stretching)[71] after the silane treatment confirms the modification that took place on the surface of the PHSC films.

The crystallinity of the HSC films before and after the surface modifications was characterized by X-ray diffraction, as shown in Figure 3b. The corresponding crystallinity index (CrI) was calculated according to the empirical Equation (1).[73] As illustrated in Figure 3b, all diffractograms exhibited two high-intensity peaks at ≈16° and 22°, which corresponded to the cellulose crystalline planes of (1–10)/(110) and (200), respectively.[74] Specifically, the peak observed at ≈16° was associated with the cellulose Iβ crystal pattern, which contained overlapping reflections of (1–10) and (110) planes.[74–76] These two peaks indicated that all HSC films retained the semicrystalline structure of cellulose even after the silane treatment,[77] which was also in agreement with the FTIR results. However, by comparison with the PHSC film, the silanized films (N_xHSC & F_yHSC) were found to have an obvious reduction in peak intensities from the distinctive cellulose Iβ (200) at 22°, and their crystallinities (CrI) were decreased by ≈10%. Since the cellulose crystalline region was caused by the inter/intramolecular hydrogen bonds from the adjacent hydroxyl groups in cellulose macromolecules,[78,79] this ordered crystalline arrangement would be greatly affected when the hydroxyl groups on the surface of PHSC films were replaced by amorphous silane hydrocarbon chains,[80] which in turn explained the reduction in the crystallinity index here. Thus, the effectiveness of the chemical treatment could be well assessed by the change in the cellulose crystallinity.

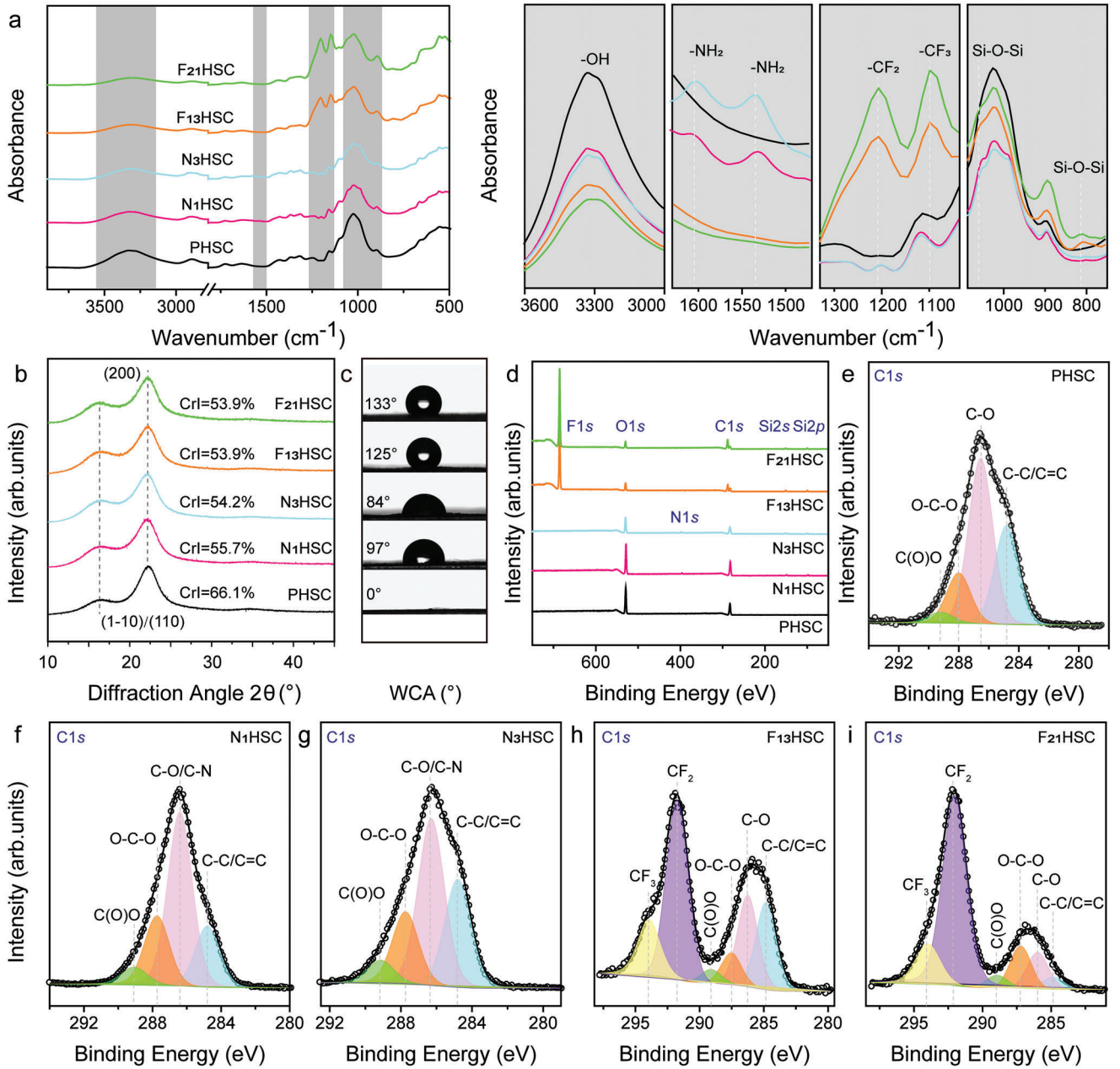

Figure 3. Characterization results of PHSC, N_1HSC, N_3HSC, F_{13}HSC, and F_{21}HSC films. a) FTIR from 4000 to 500 cm^{-1}. b) XRD spectra. c) Water contact angles. d) Wide scan XPS spectra. e–i) Detailed C1*s* spectra.

The hydrophilicity and hydrophobicity of all HSC films were evaluated by water contact angle measurements, as depicted in Figure 3c. For friction materials, their surface hydrophobicity hierarchy was found to be tightly correlated with their surface polarizability and work function, which would further influence the amount of transfer charge and the corresponding TENG's output performance.[81,82] Figure 3c depicts the clear changes in the contact angle of PHSC before and after surface modification. The PHSC was evaluated as hydrophilic since it showed a WCA of 0°, which was consistent with its abundant hydroxyl groups (Figure 3a) and porous structure (Figure 2f). However, after the silane treatment, HSC films grafted with different silanes (N_xHSC & F_yHSC) displayed an obvious hydrophobicity variation. Apart from the effect of surface roughness (Figure 2i–l), the wettability of the modified surface was mainly determined by the outermost layer; as a result, the variation in the WCA value observed here was due to differences in electronic properties among different types of silanes.[81] Specifically, the WCA decreased from 97° (N_1HSC) to 84° (N_3HSC) when PHSC was grafted with an increased amount of amine groups. Similar decrease in WCA can be found in the reported aminosilane surface characterization, where the WCA of coated silicon oxide surface decreased from 65° to 45° with an increased amount of amine groups.[83] In contrast, the WCA showed a different increase in F_yHSC from

Table 1. Types and distribution of C bonds on all HSC films.

Sample	C_1 C—C/C=C 284.8 eV [%]	C_2 C—O/C—N 286.0 eV [%]	C_3 O—C—O 287.2 eV [%]	C_4 O—C=O 289.0 eV [%]	CF_2 291.7 eV [%]	CF_3 294.0 eV [%]
PHSC	30.6	50.8	15.4	3.2	–	–
N_1HSC	19.1	54.2	21.4	5.3	–	–
N_3HSC	29.3	45.1	19.5	6.1	–	–
F_{13}HSC	18.6	19.5	6.8	3.0	38.4	13.7
F_{21}HSC	3.2	9.3	10.8	3.2	60.9	12.6

125° (F_{13}HSC) to 133° (F_{21}HSC), indicating enhanced hydrophobicity with additional fluorine-rich groups (—CF_2 & —CF_3).[84,85] Since the functional group with amine (—NH_2) has the lowest tendency to attract electrons, while fluoro (—F) has the highest tendency,[86–88] their different electronegativities of atoms on silane had a considerable impact on the free energy as well as the polarizability of the friction surface,[89] which plays an important role in their corresponding surface wettability and work function when utilized in TENG devices.[82,88]

zXPS was employed for qualitative and semiquantitative analysis of the elements and chemical structures on various HSC film surfaces before and after silanization. In addition to the peaks referring to O1*s* and C1*s* on PHSC,[24,69] four newly appeared peaks could be found on the surface of N_xHSC and F_yHSC, which were detected as N1*s*, F1*s*, Si1*s*, and Si2*p*, respectively (see Figure 3d).[24,69,90] The summarized element proportions of all samples are also shown in Table S2, Supporting Information, which showed clear increases in the nitrogen and fluoride proportions of N_xHSC and F_yHSC, respectively. Moreover, the successful modification of HSC films can also be confirmed with the results of the high-resolution C1*s* narrow scan spectra (Figure 3e–i). Four peaks representing different types of carbon bonds, namely, C—C/C=C (284.8 eV), C—O/C—N (286.0 eV), O—C—O (287.2 eV), and O—C=O (289.0 eV), were all observed in the spectra of PHSC (Figure 3e) N_xHSC (Figure 3f,g), and F_yHSC (Figure 3h,i), while the peak at 286.0 eV on F_yHSC surface refers only C–O due to different silanizations.[90] For the spectra of F_yHSC (Figure 3h,i), two additional peaks at 291.7 and 294.0 eV could be found in addition to the abovementioned four peaks, indicating the present of —CF_2 and —CF_3, respectively.[69] Given that the relative spectral intensities are propotional to the abundance of the corresponding bonds within the volume probed by XPS, the calculated proportions of all carbon bonds are listed in **Table 1**. Here, PHSC and N_xHSC were all dominated by the C_2-type carbon bond, as the peaks of C—O and C—N overlapped. The modification of amine-bearing silane chains onto the PHSC surface could be further confirmed in the high-resolution N1*s* spectrum of N_xHSC (Figure S2, Supporting information).[90] In addition, as the proportion of C—O bonds dramatically decreased from 50.8% (PHSC) to 19.5% (F_{13}HSC), the ratio of newly generated —CF_2 and —CF_3 bonds within F_{13}HSC increased. In addition, the ratio of C_2-type carbon bonds experienced a further reduction to 9.3% (F_{21}HSC), which was attributed to the fluorine-rich silane chains of FTCS covering the modified surface. The differences in the carbon bond ratio (Table 1) among all tested HSC films were not only consistent with the previously observed FTIR results (Figure 3a) but also related to the varied WCA values (Figure 3c). These results confirmed the successful surface modification of PHSC films and laid a solid foundation for analyzing different HSC-TENG performances.

To apply the fabricated various HSC films in energy harvesting, a typical contact-separation mode was utilized to realize HSC-TENGs, as shown in **Figure 4**. N_xHSC and F_yHSC were applied as the positive and negative friction layers, respectively. Ag nanowires were drop-casted on both N_xHSC and F_yHSC as back electrodes and connected to the external circuit for measuring the electrical output. The working principle of the HSC-TENG is based on contact electrification and electrostatic induction,[91] as schematically illustrated in Figure 4. After several cycles of friction between the two triboelectric layers (N_xHSC and F_yHSC), electrons transfer from the surface of N_xHSC to F_yHSC due to their different electron affinities. Here, amino groups can help N_xHSC lose electrons more easily, while fluoro groups improve the tendency of F_yHSC to gain electrons during contact electrification. Specifically, when they were in contact (state I), there was no current across the two back electrodes due to electrostatic equilibrium. While they started separating from each other (stage II), electrons flowed through the external circuit from the top electrode to the bottom electrode to balance their potential differences due to the electrostatic induction effect. This electron flow could last until the friction layers were completely separated (state III), where a new electrostatic equilibrium was established. Similarly, when they were in contact again (state IV), electrons flowed back from the bottom electrode to the top electrode, resulting in a reverse current pulse. In this way, the performance of various films as friction layers in HSC-TENGs can be evaluated with their electrical signals.

To investigate the effects of the stellate structure on the electrical output of the cellulose-based TENG, two cellulose films (PHSC & HEC) with different surface structures were tested as positive friction layers. The output of the corresponding PHSC-TENG and HEC-TENG were generated by pressing the cellulose films onto a vertically aligned negative triboelectric surface of random electrospun PVDF films. Their open-circuit voltages (V_{OC}), short-circuit currents (I_{SC}) and short-circuit transferred charges (Q_{SC}) under varying forces with a working frequency of 0.5 Hz are compared in **Figure 5**.

Generally, the electrical outputs of the PHSC-TENG and HEC-TENG presented a similar increasing trend with increasing contact forces, which was attributed to the increased effective contact areas of the friction layers with enhanced contact forces.[26] However, when the applied external forces increased from 70 to

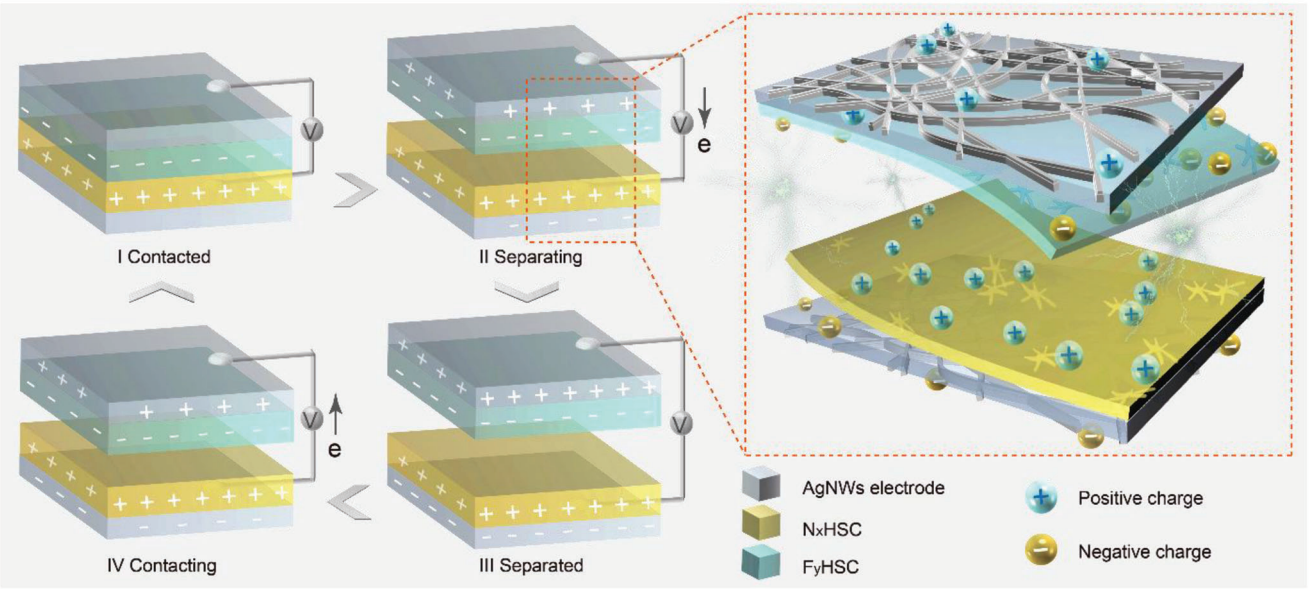

Figure 4. Schematic illustration of the working principle of HSC-TENGs.

80 N, the corresponding electrical output of the PHSC-TENG and HEC-TENG demonstrated obviously different degrees of increase. For instance, the V_{OC} of the PHSC-TENG increased significantly from 81 (70 N) to 98 V (80 N), while that of the HEC-TENG remained the same (39 V) as shown in Figure 5a. This implied that the output saturation of the HEC-TENG occurred within ≈60–70 N, suggesting that the PHSC-TENG may have the potential to harvest mechanical energy under a wider range of forces. Moreover, the PHSC-TENG contained relatively higher electrical outputs, which were above twice as high as those of the flatter cellulose film-based HEC-TENG under all varied forces. Therefore, the electrical performance of traditional flat cellulose-based TENGs can be improved with the rougher surface of HSCUs.[35] When compared with the V_{OC} of the reported TENG (60 V) based on similar-structured cellulose (TEMPO-oxidized cellulose aerogel) and PVDF (random electrospun PVDF) films,[26] the V_{OC} of the PHSC-TENG (67 V) was also 12% higher under the same external force of 10 N. This similar electrical output enhancement can also be found in the reported TENG with optimized fiber porosity design,[36] where the fabricated nanoscale inner pores within each electrospun fiber served as induced charge traps for the higher surface charge density. Thus, the higher electrical output performance of the PHSC-TENG here can be attributed to the hollow stellate structure and the nanoporous surface of HSCUs.[36] HSCU structure-derived porosity and delignification caused by nanopores can largely enhance the surface roughness on the friction surface, resulting in an increased effective contact area. On the other hand, the inner pores of PHSC films were considered to be advantageous for the accumulation of induced charges for further promotion of surface charge density.[36] Hence, this PHSC film derived from biomass offers great potential as an alternative material for constructing cellulose-based TENGs. Its distinctive structure not only enhances surface roughness and porosity but also provides a lightweight and flexible cellulosic substrate for the friction layers in TENGs. Therefore, in order to realize the all-in-one hollow stellate cellulose-based TENGs (HSC-TENGs) meanwhile avoid using petroleum-based, nonrecyclable organic friction materials,

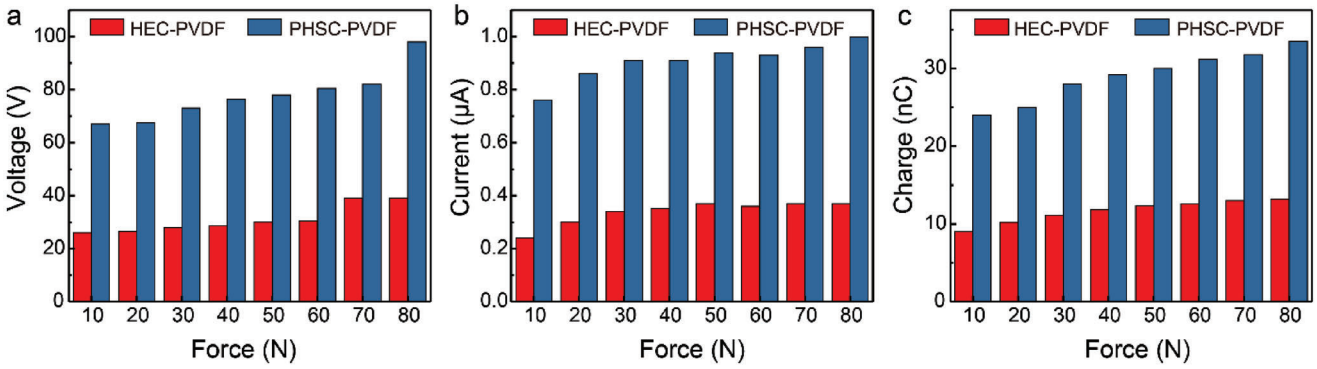

Figure 5. Comparisons of the essential electrical characteristics between the HEC-TENG and PHSC-TENG. a) Open-circuit voltage, b) short-circuit current, and c) short-circuit transferred charges under different forces (10 to 80 N) with a working frequency of 0.5 Hz.

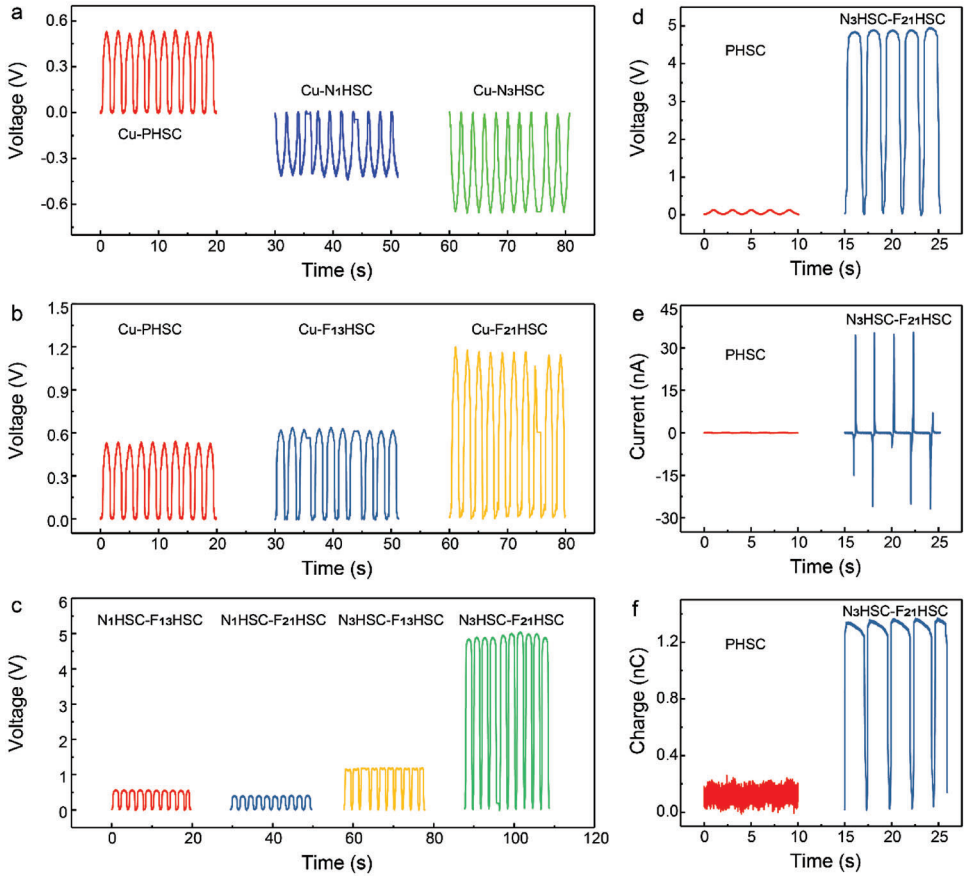

Figure 6. Open-circuit voltages of a) Cu-N_xHSC TENGs, b) Cu-F_yHSC TENGs and c) N_xHSC-F_yHSC TENGs. d–f) Open-circuit voltages, short-circuit current and short-circuit transferred charges of the PHSC-PHSC TENG and N3HSC-F21HSC TENG.

PHSC films were further silanized as both positive (N_xHSC) and negative friction layers (F_yHSC). The utilization of silane coupling agents in natural fiber modification is widely used due to their cost-effectiveness, simplicity, competitive specific mechanical properties, and environmental friendliness.[92] By incorporating drop-casted AgNWs electrode, N_xHSC and F_yHSC can simultaneously serve as the triboelectric layer, inductive electrode and substrate at the same time, thereby ensuring a more sustainable cellulosed-based TENG.

To assess the effects of amine and fluorine content on the triboelectric polarities of modified HSC films, Cu foils were utilized here as the comparison friction material.[10] Specifically, by connecting the electrometer's negative probe to the AgNWs back electrodes on various HSCs, their triboelectric polarities can thus be compared with Cu foils attached on the positive probe within the corresponding HSC-TENGs (0.5 Hz, 50 N). As shown in **Figure 6**a, the negatively charged PHSC can be tuned to be positively charged after grafting with amino groups. This phenomenon can be attributed to the strong electron-donating ability from the lone pairs of electrons presented in -NH_2 functional groups.[93] Consequently, the tribopositivity of N_xHSC can be further improved by grafting an increased content of amino groups.[94] For instance, the V_{OC} of the Cu-N_3HSC TENG (−0.68 V) was 1.6 times that of Cu-N_1HSC TENG (−0.42 V), indicating its stronger electron donating functionality. In addition, the secondary amine (R_2NH) in N_3HSC further contributed to its tribopositivity improvement, as the ability to lose electrons is positively correlated with the alkalinity strength of a compound.[95] This change in the tribopositivity was consistent with the reported order of alkalinity for aliphatic amines in the gas phase ($R_3N > R_2NH > RNH_2$).[96]

Similarly, the tribonegativity of fluorinated HSC films (F_yHSC) can be improved (Figure 6b) by grafting a higher content of fluorine groups because of the high electronegativity of the F atoms in the -CF_2/-CF3 group.[95] Taking the Cu-F_{21}HSC TENG as an example, the V_{OC} value (1.18 V) obviously outperformed that of the Cu-F_{13}HSC TENG (0.64 V), as F_{21}HSC contained denser -CF_2/-CF_3 groups on its surface. In other words, the triboelectric polarities of PHSC films can be successfully tuned by controlling the amount of amino/fluorine-bearing functional groups introduced onto their surface, which is consistent with various characterization results shown in Figure 5. In this system, the N_3HSC-F_{21}HSC TENG (also marked as N_3F_{21}-TENG hereafter) achieved the highest V_{OC} (4.86 V) in comparison with other HSC-TENGs (Figure 6c), as it combined two HSC friction layers of highest tribopositivity (N_3HSC) and tribonegativity (F_{21}HSC). Figure 6d–f clearly demonstrate the superior performance of the N_3F_{21}-TENG compared to TENGs using two pristine HSC films as triboelectric layers (PHSC-TENG). The N_3F_{21}-TENG exhibited significantly higher values for V_{OC}, I_{SC},

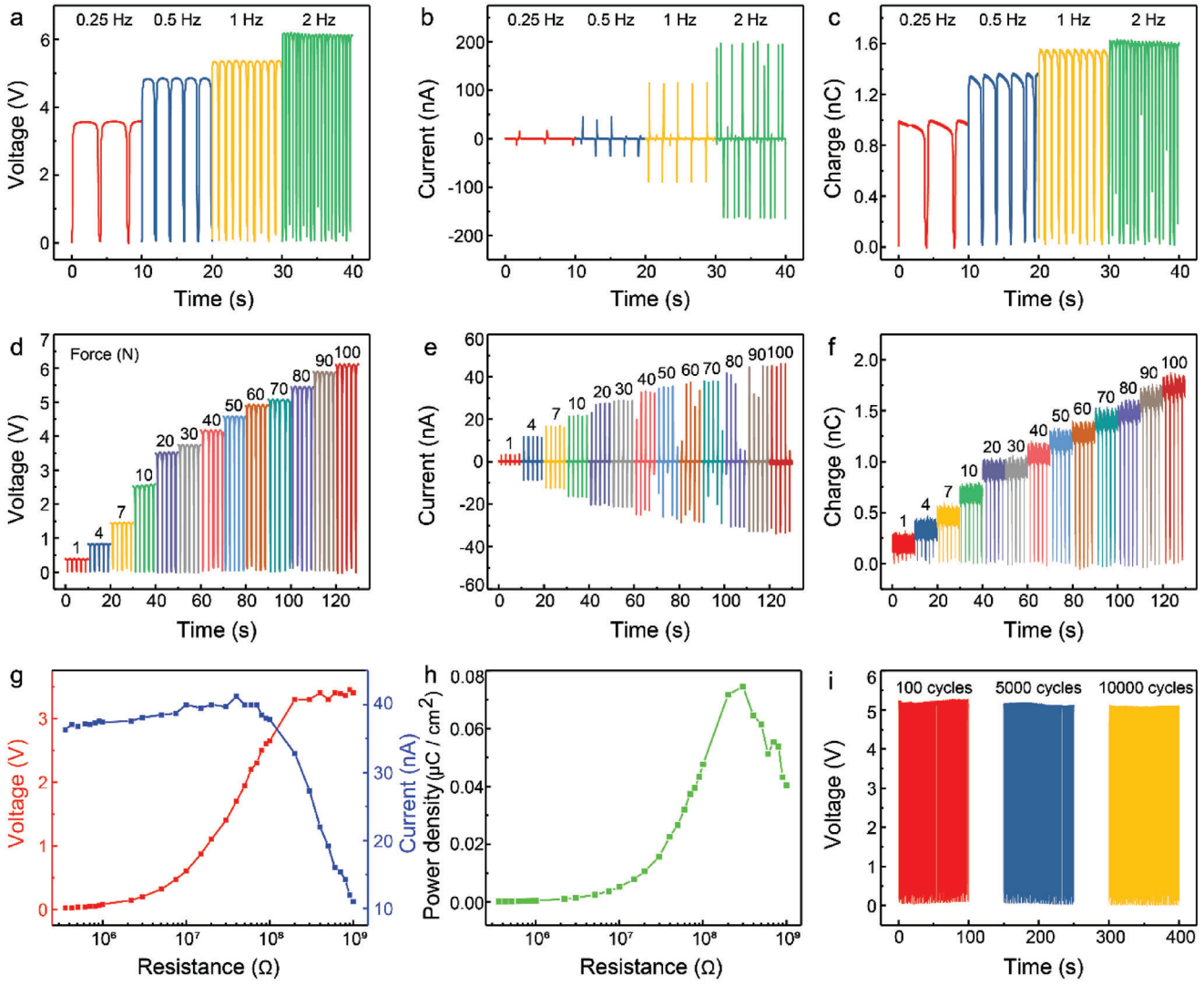

Figure 7. The electrical output performance of N_3F_{21}-TENG under different working frequencies and forces. a–c) Open-circuit voltages, short-circuit currents and short-circuit transferred charges under different working frequencies. d–f) Open-circuit voltages, short-circuit currents and short-circuit transferred charges under different load forces. g) Dependence of the output current and voltage of the N_3F_{21}-TENG on the external load resistances. h) The instantaneous power output of N_3F_{21}-TENG on external load resistances. i) Stability of N_3F_{21}-TENG.

and Q_{SC} outputs. In fact, the output V_{OC} of the N_3F_{21}-TENG was enhanced by a factor of 28 compared to the PHSC-TENG. This great enhancement of N_3F_{21}-TENG can also be attributed to the inner pores of N_3HSC and F_{21}HSC, which acted as the induced charge traps,[36] leading to an increased trap density that can effectively prevent the dissipation of the trapped triboelectric charges into the environment.[97] These results validate the significant impact of the amine and fluorine content on the triboelectric polarities of the modified HSC films.[93] In addition, N_3F_{21}-TENG also showed a comparable voltage output as the ones compared with other representative works on all-cellulose-based TENGs (Table S3, Supporting information). Considering the needs for biodegradability and lightweight of all materials (triboelectric materials and electrodes) for future wearable TENGs, the N_3F_{21}-TENG contains none petroleum-based synthetic polymers, and the used PHSC with natural lightweight, porosity and rough surface also makes it a promising alternative to synthetic cellulose aerogel films. Furthermore, building upon researchers' previous explorations of cellulose-based TENGs, the electrical performance of HSC-TENGs holds considerable potential to be further enhanced through various methods as highlighted in Table S3, Supporting Information, including varying contact friction materials,[26,33,98] increasing contact surface area,[98] optimizing material thickness,[98,99] enhancing surface roughness,[100,101] grafting high-polarity functional groups,[102] incorporating additives,[103–105] and optimizing TENG structures.[106,107] These corresponding potential optimizations awaits researchers' future explorations. Here, this N_3F_{21}-TENG was subsequently tested under different external conditions to further investigate its output performance.

As shown in **Figure 7**, the output performance of the N_3F_{21}-TENG was further investigated with respect to the key

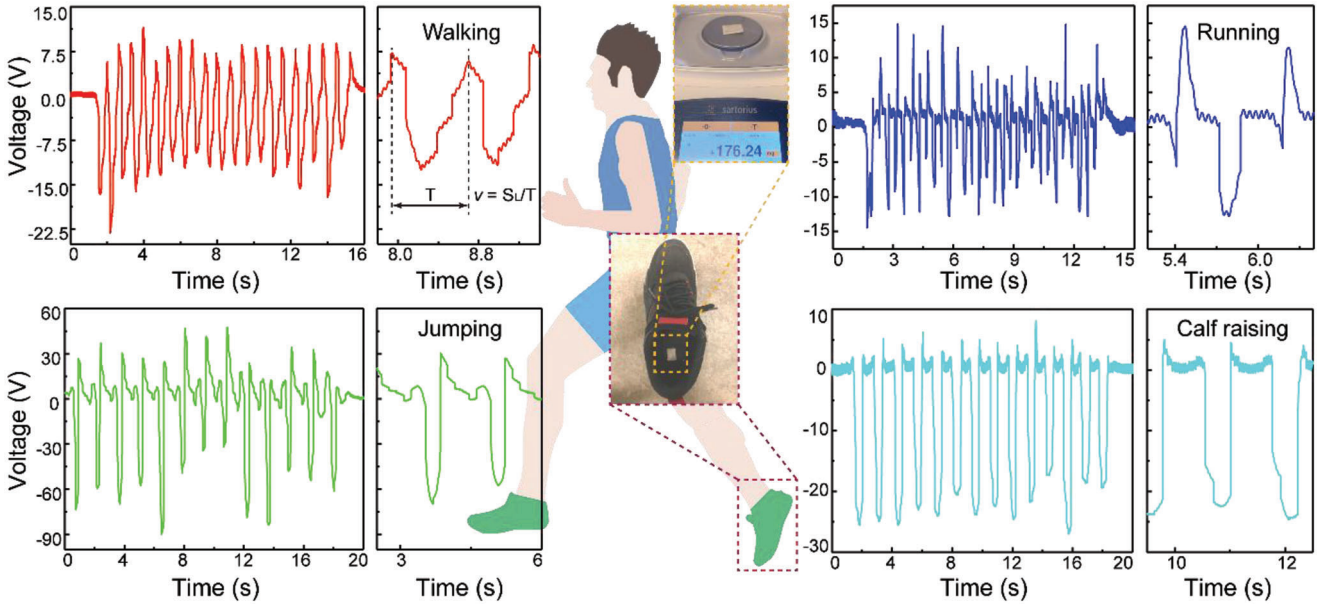

Figure 8. Monitoring results of N_3F_{21}-TENG as a self-powered triboelectric sensor in different body motions of walking, running, jumping, and calf raising.

influencing factors (e.g., working frequency, applied load force and external load resistance). In general, the V_{OC}, I_{SC}, and Q_{SC} of the N_3F_{21}-TENG (Figure 7a–c) all showed an obvious upward trend as the working frequency increased from 0.25 to 2 Hz (50 N). It is worth noting that V_{OC} and Q_{SC} in TENGs usually maintain stable outputs at various frequencies, while V_{OC} and Q_{SC} of N_3F_{21}-TENGs both show an apparent increase under different working frequencies. This obvious output improvement was contributed by the unique porous structure of HSCUs, as it might trap and store more charges under a higher excitation frequency.[10] When the contact frequency remained constant at 0.5 Hz, the output performance of the N_3F_{21}-TENG was tested by applying different external forces. As output saturation of the PHSC-TENG was not observed within ≈10–80 N (Figure 5), the PHSC film in the friction layer may have the potential to harvest mechanical energy under a wider range of forces. In order to gain a comprehensive understanding of the performance limits of N_3F_{21}-TENG and to ensure its functionality under various working conditions, a wider range of forces (1 to 100 N) was applied. The selection of this force range was also guided by the peak force we measured (96.5 N) as illustrated in Figure S3, Supporting Information, as well as the reported peak pressures observed in the heel regions at varying gait speeds (5, 6.5, and 9 km h^{-1}), ranging from 22.9 ± 10.2 to 38.9 ± 6.3 N cm^{-2}.[108] As shown in Figure 7d, when the applied forces became stronger, the V_{OC}, I_{SC}, and Q_{SC} (Figure 7d–f) of the N_3F_{21}-TENG all responded well with a continuous enhancement accordingly. For instance, the V_{OC} of N_3F_{21}-TENG increased dramatically from 0.43 (1 N) to 6.23 V (100 N), which can be attributed to the roughness providing an increased contact area with enhanced forces. This improved friction area of N_3HSC and F_{21}HSC with strengthened contacting force was also in accordance with previously characterized surface roughness. Furthermore, the impedance matching of N_3F_{21}-TENG with different external load resistances was investigated, as shown in Figure 7g. As the load resistance increased, the voltage increased gradually and then remained stable, whereas the current first showed no change but subsequently decreased. According to Figure 7h, the internal resistance of the N_3F_{21}-TENG was speculated to be 300 MΩ because its maximum calculated instantaneous output power density was found under an external resistance of 300 MΩ. Overall, benefiting from the supportive porous structure and intrinsic surface roughness, the N_3F_{21}-TENG has a wide range of applicable forces/frequencies and long-term stability over 10 000 cycles (Figure 7i), which together lay a solid foundation for its further practical applications as a self-powered triboelectric sensor.

In view of the lightness, flexibility, and long-term stability of the N_3F_{21}-TENG, the reliability of N_3F_{21}-TENG working as a self-powered triboelectric sensor (N_3F_{21}-SPTS) for gait analysis was further evaluated based on its output under different body motions (e.g., walking, running, jumping, and calf raising) with the same volunteer. During the test, as shown in **Figure 8**, the lightweight wearable N_3F_{21}-SPTS (176.2 mg) was tightly attached to the shoes under the heel region of the foot. This foot region was selected due to the reported good repeatability (ICC > 0.9) of peak pressures observed in the heel regions during different gait speeds (5, 6.5, and 9 km h^{-1}),[108] which was speculated to be favorable for the good repeatability of the output signals.

The signal outputs obtained from N_3F_{21}-SPTS under different motion states were presented in Figure 8. Obviously, the N_3F_{21}-SPTS can be successfully activated and demonstrated a stable output performance during the process of all activities including walking, running, jumping, and calf raising. However, the observed peak V_{OC} acquired by different motion showed significant differences. In comparison, the highest of 47.14 V was acquired by the jumping activity, while the locomotion of walking, running, and calf raising generated a lower peak V_{OC} of 11.49, 14.46, and 5.23 V, respectively. This output voltage

difference can be attributed to the varying forces and frequencies of the heel pressing on N_3F_{21}-SPTS during different motions. Notably, this rising trend of the V_{OC} at walking, running, and jumping was found to align with previous findings on corresponding associated plantar pressures, which was 14.1 ± 2.1, 31.8 ± 4.1, and 40.3 ± 3.3 N cm^{-2}, respectively.[109] These monitoring results were also consistent with previous investigations (Figure 7) regarding the high correlation between the output of N_3F_{21}-SPTS and applied pressures.

Meanwhile, the output signals of N_3F_{21}-SPTS was also valuable for monitoring various physical parameters in gait analysis, such as plantar motion features,[110,111] step counts,[112] and motion speed.[113] These parameters are essential for assessing athletic performance and guiding training adjustments. Taking the walking motion as an example, the corresponding signal generated by N_3F_{21}-SPTS (Figure 8) showed a distinct pattern that consisted of an initial raising positive peak, corresponding to the foot condition from "heel contact" to "toe contact," followed by a subsequent negative peak representing the transition from "heel leave" to "toe leave."[112] Due to the relatively longer contact time and gradually increased pressure between heel and N_3F_{21}-SPTS during the condition from "heel contact" to "toe contact," the voltage output of the N_3F_{21}-SPTS displayed a stepwise rising shape in its positive peak. In contrast, running entailed shorter contact time between heel and N_3F_{21}-SPTS, resulting in the sharper positive peaks in the signal.[114] Regarding the voltage output produced during jumping and calf raising, both activities exhibited two separate small peaks within their positive peaks. These two peaks were associated with the impact force during "heel landing" and the subsequent ground reaction force to the sole.[111] Based on this, we can further analyze and detect the user's activities and gait patterns by extracting features from voltage values and fluctuation frequencies. Specifically, the number of voltage peaks can be utilized to represent step counts,[111] and the time interval between voltage peaks, representing the frequency of the signal, can be employed to sense the motion speed. The motion speed can be calculated from the equation $v = S_L/T$, where T represents the time interval between two positive voltage peaks, and S_L denotes the stride length of a walking cycle.[110,112]

Furthermore, in order to elucidate the performance stability of the N_3F_{21}-SPTS device for gait analysis, a long-duration test was conducted by placing the device inside a shoe and wearing it continuously for 24 h. Throughout this entire day, various daily activities such as standing, walking, and cycling were performed, resulting in a total step count of 10 389. Here, each step corresponds to one contact-separation cycle of the N_3F_{21}-SPTS device. As shown in Figure S4, Supporting information, N_3F_{21}-SPTS demonstrated a notable similarity in the output signals before and after 10 389 cycles (24 h) for various body motions. At the same time, these signals maintained distinct positive voltage peak patterns among different movements, indicating the device's ability to accurately distinguish and analyze different motions during gait analysis. This good responsiveness of voltage signals to the different motions can be attributed to the porous structure within the friction layers.[115] While a decrease of output voltages in the N_3F_{21}-SPTS signals was observed after 24 h utilization. Since a stable electrical output performance of the N_3F_{21}-SPTS can be obtained under perpendicular force for 10 000 cycles (Figure 7i), this decrease in output voltage was speculated to be caused by the complex environment within the shoe, including factors such as moisture, dirt, shear force,[116] or compressed foam tape spacer.

Despite the decrease in voltage output, the signals generated by N_3F_{21}-SPTS after 24 h still exhibited excellent signal resolution with clear characteristic positive voltage peaks. This signal resolution is more crucial for precise gait analysis, enabling the extraction of essential parameters such as plantar motion features, step counts, and motion speed, rather than relying solely on voltage output values.[110,111,117] The findings demonstrated that the N_3F_{21}-SPTS can sustain recognizable output signals with excellent resolution over 10 000 cycles in practical conditions. These results highlight its potential for practical implementation in gait analysis and offer valuable insights and recommendations for the future of TENG devices' optimizations for gait analysis in the future. Therefore, N_3F_{21}-TENG can not only be applied as a sensor with sufficient stable voltage output for distinguishing different body motion states but also be regarded as potential feedback for personal sports or in-depth analysis for athletes' daily training activities. The study was approved by the Research Ethics Review Committee (CETO) at the Faculty of Arts, University of Groningen and informed written consent was also obtained from the volunteer.

3. Conclusion

In conclusion, the hollow stellate cellulose-based TENGs (HSC-TENGs) proposed in this study demonstrated remarkable performance in terms of output voltage and stability. The unique hollow stellate cellulose units (HSCUs) derived from the aerenchyma of *Juncus effusus* L. contributed to the enhanced surface roughness, porosity and lightness of the HSC films, which resulted in improved triboelectric polarities that could be further controlled by modification of the amino/fluorine-bearing groups. Specifically, the N_3F_{21}HSC-TENG, modified with amino/fluorine-bearing groups, achieved a high output voltage of 4.86 V, which was 28 times higher than that of the TENG utilizing two pristine hollow stellate cellulose films (PHSCs) as triboelectric layers. Moreover, the lightweight N_3F_{21}-TENG (176.2 mg) was successfully employed as a wearable self-powered triboelectric sensor for various different body motion states, such as walking, running, jumping, and calf raising, with excellent signal resolution over 10 000 cycles in practical conditions for precise gait analysis. Finally, this cellulose-based TENG not only holds great potential for future wearable in-depth body locomotion analysis but also presents opportunities for utilizing various aerenchyma structures from abundant problematic aquatic or wetland weeds as a promising structural template in multifunctional cellulose-based applications.

Supporting Information

Supporting Information is available from the Wiley Online Library or from the author.

Acknowledgements

The authors would like to thank the financial support from the China Scholarship Council (CSC No. 201706300134) and the University of Groningen.

The authors would like to thank the financial support from the Advanced Materials research program of the Zernike National Research Centre under the Bonus Incentive Scheme (BIS) of the Dutch Ministry for Education, Culture and Science. The authors are deeply grateful to Dr. Rui Li (group of Polymer Chemistry and Bioengineering, University of Groningen) for his support on the water contact angle measurement. The authors are thankful to Jacob Baas (group of Nanostructures of Functional Oxides, University of Groningen) for training and access to the XRD instrument.

Conflict of Interest

The authors declare no conflict of interest.

Author Contributions

Q.C. and W.L. contributed equally to this work. Q.C.: Conceptualization, methodology, resources, formal analysis, investigation, writing – original draft. W.L.: Conceptualization, methodology, resources, TENG analysis, investigation, writing – review & editing. F.Y.: XPS measurements, investigation, writing – review & editing. D.M.: Figure optimization, investigation, writing – review & editing. J.van D.: Methodology, investigation, writing – review & editing. Y.P.: Supervision, resources, funding acquisition, writing – review & editing. P.R.: Supervision, resources, funding acquisition, writing – review & editing. K.L.: Conceptualization, supervision, resources, funding acquisition, writing – review & editing.

Data Availability Statement

The data that support the findings of this study are available from the corresponding author upon reasonable request.

Keywords

aerenchyma, biomass, cellulose films, *Juncus effusus* L., triboelectric nanogenerators

Received: May 1, 2023
Revised: July 28, 2023
Published online: September 12, 2023

[1] Z. Li, Q. Zheng, Z. L. Wang, Z. Li, *Research* **2020**, *2020*, 1.
[2] Z. Liu, H. Li, B. Shi, Y. Fan, Z. L. Wang, Z. Li, *Adv. Funct. Mater.* **2019**, *29*, 1808820.
[3] E. P. Gilshteyn, S. A. Romanov, D. S. Kopylova, G. v. Savostyanov, A. S. Anisimov, O. E. Glukhova, A. G. Nasibulin, *ACS Appl. Mater. Interfaces* **2019**, *11*, 27327.
[4] K. Guk, G. Han, J. Lim, K. Jeong, T. Kang, E. K. Lim, J. Jung, *Nanomaterials* **2019**, *9*, 813.
[5] J. Li, Y. Long, X. Wang, *Chem. Res. Chin. Univ.* **2020**, *36*, 41.
[6] Z. Wang, Z. Hao, S. Yu, C. G. de Moraes, L. H. Suh, X. Zhao, Q. Lin, *Adv. Funct. Mater.* **2019**, *29*, 1905202.
[7] J. Liu, L. Gu, N. Cui, Q. Xu, Y. Qin, R. Yang, *Research* **2019**, *2019*, 1091632.
[8] H. J. Kim, E. C. Yim, J. H. Kim, S. J. Kim, J. Y. Park, I. K. Oh, *Nano Energy* **2017**, *33*, 130.
[9] F. R. Fan, W. Tang, Z. L. Wang, *Adv. Mater.* **2016**, *28*, 4283.
[10] H. Zou, Y. Zhang, L. Guo, P. Wang, X. He, G. Dai, H. Zheng, C. Chen, A. C. Wang, C. Xu, Z. L. Wang, *Nat. Commun.* **2019**, *10*, 1427.
[11] Y. C. Lai, J. Deng, S. L. Zhang, S. Niu, H. Guo, Z. L. Wang, *Adv. Funct. Mater.* **2017**, *27*, 1604462.
[12] Z. Lin, J. Yang, X. Li, Y. Wu, W. Wei, J. Liu, J. Chen, J. Yang, *Adv. Funct. Mater.* **2018**, *28*, 1704112.
[13] K. Xia, Z. Zhu, H. Zhang, Z. Xu, *Appl. Phys. A* **2018**, *124*, 520.
[14] P. Bai, G. Zhu, Q. Jing, J. Yang, J. Chen, Y. Su, J. Ma, G. Zhang, Z. L. Wang, *Adv. Funct. Mater.* **2014**, *24*, 5807.
[15] Q. Guan, G. Lin, Y. Gong, J. Wang, W. Tan, D. Bao, Y. Liu, Z. You, X. Sun, Z. Wen, Y. Pan, *Busshitsu Kogaku Kogyo Gijutsu Kenkyusho Hokoku* **2019**, *7*, 13948.
[16] H. Kang, C. Zhao, J. Huang, D. H. Ho, Y. T. Megra, J. W. Suk, J. Sun, Z. L. Wang, Q. Sun, J. H. Cho, *Adv. Funct. Mater.* **2019**, *29*, 1903580.
[17] Y. Lee, J. Kim, B. Jang, S. Kim, B. K. Sharma, J. H. Kim, J. H. Ahn, *Nano Energy* **2019**, *62*, 259.
[18] K. Meng, J. Chen, X. Li, Y. Wu, W. Fan, Z. Zhou, Q. He, X. Wang, X. Fan, Y. Zhang, J. Yang, Z. L. Wang, *Adv. Funct. Mater.* **2019**, *29*, 1806388.
[19] H. J. Qiu, W. Z. Song, X. X. Wang, J. Zhang, Z. Fan, M. Yu, S. Ramakrishna, Y. Z. Long, *Nano Energy* **2019**, *58*, 536.
[20] M. O. Shaikh, Y. bin Huang, C. C. Wang, C. H. Chuang, *Micromachines* **2019**, *10*, 438.
[21] X. Lan, W. Li, C. Ye, L. Boetje, T. Pelras, F. Silvianti, Q. Chen, Y. Pei, K. Loos, *ACS Appl. Mater. Interfaces* **2023**, *15*, 4398.
[22] D. Maniar, C. Fodor, I. K. Adi, A. J. J. Woortman, J. van Dijken, K. Loos, *Polymers* **2021**, *70*, 555.
[23] Y. Song, Z. Shi, G. H. Hu, C. Xiong, A. Isogai, Q. Yang, *J. Mater. Chem. A* **2021**, *9*, 1910.
[24] S. Nie, C. Cai, X. Lin, C. Zhang, Y. Lu, J. Mo, S. Wang, *ACS Sustainable Chem. Eng.* **2020**, *8*, 18678.
[25] R. J. Moon, A. Martini, J. Nairn, J. Simonsen, J. Youngblood, *Chem. Soc. Rev.* **2011**, *40*, 3941.
[26] Y. Song, J. Bao, Y. Hu, H. Cai, C. Xiong, Q. Yang, H. Tian, Z. Shi, *Sustainable Energy Fuels* **2022**, *6*, 2377.
[27] A. Isogai, T. Saito, H. Fukuzumi, *Nanoscale* **2011**, *3*, 71.
[28] S. Elazzouzi-Hafraoui, Y. Nishiyama, J. L. Putaux, L. Heux, F. Dubreuil, C. Rochas, *Biomacromolecules* **2008**, *9*, 57.
[29] K. M. Gupta, J. Jiang, *Chem. Eng. Sci.* **2015**, *121*, 180.
[30] T. Rosenau, A. Potthast, H. Sixta, P. Kosma, *Prog. Polym. Sci.* **2001**, *9*, 1763.
[31] Q. Yang, X. Qin, L. Zhang, *Cellulose* **2011**, *18*, 681.
[32] J. Cai, L. Zhang, *Macromol. Biosci.* **2005**, *5*, 539.
[33] M. Wang, W. Li, C. You, Q. Wang, X. Zeng, M. Chen, *RSC Adv.* **2017**, *7*, 6772.
[34] C. Qian, L. Li, M. Gao, H. Yang, Z. Cai, B. Chen, Z. Xiang, Z. Zhang, Y. Song, *Nano Energy* **2019**, *63*, 103885.
[35] H. Y. Mi, X. Jing, Q. Zheng, L. Fang, H. X. Huang, L. S. Turng, S. Gong, *Nano Energy* **2018**, *48*, 327.
[36] B. Yu, H. Yu, T. Huang, H. Wang, M. Zhu, *Nano Energy* **2018**, *48*, 464.
[37] Y. Shao, C. ping Feng, B. wen Deng, B. Yin, M. Bo Yang, *Nano Energy* **2019**, *62*, 620.
[38] R. D. Tweed, N. Woodhead, *J. Ecol.* **1946**, *33*, 210.
[39] A. Lazenby, *J. Ecol.* **1955**, *43*, 595.
[40] W. Kaczmarek-derda, J. Folkestad, M. Helgheim, J. Netland, K. A. Solhaug, L. O. Brandsaeter, *Weed Res.* **2014**, *54*, 603.
[41] G. N. Ervin, R. G. Wetzel, *Oecologia* **2002**, *130*, 626.
[42] B. C. Wolverton, R. C. Mcdonald, *Ambio* **1979**, *8*, 2.
[43] W. Kaczmarek-derda, L. Østrem, M. Myromslien, L. O. Brandsaeter, J. Netland, *Weed Res.* **2019**, *59*, 67.
[44] S. Blossfeld, D. Gansert, B. Thiele, A. J. Kuhn, R. Lösch, *Soil Biol. Biochem.* **2011**, *43*, 1186.
[45] S. H. F. W. Justin, W. Armstrong, *New Phytol.* **1987**, *106*, 465.
[46] L. Xia, S. Zhou, C. Zhang, Z. Fu, A. Wang, Q. Zhang, Y. Wang, X. Liu, X. Wang, W. Xu, *J. Clean Prod.* **2020**, *259*, 120812.

[47] J. Sun, H. Guo, J. Ribera, C. Wu, K. Tu, M. Binelli, G. Panzarasa, F. W. M. R. Schwarze, Z. Lin Wang, I. Burgert, *ACS Nano* **2020**, *14*, 14665.
[48] B. P. Calabia, F. Ninomiya, H. Yagi, A. Oishi, K. Taguchi, M. Kunioka, M. Funabashi, *Polymers* **2013**, *5*, 128.
[49] B. Sun, J. Zhao, T. Wang, Y. Li, X. Yang, F. Tan, Y. Li, C. Chen, D. Sun, *Carbohydr. Polym.* **2023**, *309*, 120664.
[50] Z. Shao, J. Sun, J. Wang, K. Lv, B. Liao, R. Wang, H. Jiang, *ACS Sustainable Chem. Eng.* **2021**, *9*, 9689.
[51] B. P. Frank, D. P. Durkin, E. R. Caudill, L. Zhu, D. H. White, M. L. Curry, J. A. Pedersen, D. H. Fairbrother, *ACS Appl. Nano Mater.* **2018**, *1*, 7025.
[52] W. Perdoch, B. Mazela, M. Tavakoli, A. Treu, *Waste Manage.* **2023**, *160*, 165.
[53] M. Chabannes, K. Ruel, A. Yoshinaga, B. Chabbert, A. Jauneau, J.-P. Joseleau, A.-M. Boudet, *Plant J.* **2001**, *28*, 271.
[54] P. Myllytie, L. Salmén, E. Haimi, J. Laine, *Cellulose* **2010**, *17*, 375.
[55] M. Wohlert, T. Benselfelt, L. Wågberg, I. Furó, L. A. Berglund, J. Wohlert, *Cellulose* **2022**, *29*, 1.
[56] H. J. Liu, K. Cho, *Appl. Phys. Lett.* **2004**, *85*, 807.
[57] H. Yousefi, M. Faezipour, S. Hedjazi, M. M. Mousavi, Y. Azusa, A. H. Heidari, *Ind. Crops Prod.* **2013**, *43*, 732.
[58] M. Imani, A. Ghasemian, M. R. Dehghani-Firouzabadi, E. Afra, M. Borghei, L. S. Johansson, P. A. C. Gane, O. J. Rojas, *Adv. Mater. Interfaces* **2019**, *6*, 1900770.
[59] K. S. Kontturi, K. Y. Lee, M. P. Jones, W. W. Sampson, A. Bismarck, E. Kontturi, *Cellulose* **2021**, *28*, 6619.
[60] C. E. Wen, Y. Yamada, K. Shimojima, Y. Chino, H. Hosokawa, M. Mabuchi, *Mater. Lett.* **2004**, *58*, 357.
[61] M. E. A. Fidelis, T. V. C. Pereira, O. D. F. M. Gomes, F. D. A. Silva, R. D. T. Filho, *J. Mater. Res. Technol.* **2013**, *2*, 149.
[62] R. G. Zhbankov, S. P. Firsov, D. K. Buslov, N. A. Nikonenko, M. K. Marchewka, H. Ratajczak, B. I. Stepanov, *J. Mol. Struct.* **2002**, *614*, 117.
[63] J. Sugiyama, J. Persson, H. Chanzy, *Macromolecules* **1991**, *24*, 2461.
[64] N. Reddy, Y. Yang, *Polymer* **2005**, *46*, 5494.
[65] M. Åkerholm, B. Hinterstoisser, L. Salmén, *Carbohydr. Res.* **2004**, *339*, 569.
[66] J. Jayaramudu, B. R. Guduri, A. Varada Rajulu, *Carbohydr. Polym.* **2010**, *79*, 847.
[67] H. Zhou, H. Zhu, F. Xue, H. He, S. Wang, *J. Chem. Eng.* **2020**, *385*, 123879.
[68] O. Somseemee, P. Sae-Oui, C. Siriwong, *Cellulose* **2022**, *29*, 8675.
[69] S. Nie, Q. Fu, X. Lin, C. Zhang, Y. Lu, S. Wang, *J. Chem. Eng.* **2021**, *404*, 126512.
[70] B. Kaynak, C. Alpan, M. Kratzer, C. Ganser, C. Teichert, W. Kern, *Appl. Surf. Sci.* **2017**, *416*, 824.
[71] K. Xie, Y. Yu, Y. Shi, *Carbohydr. Polym.* **2009**, *78*, 799.
[72] M. de Oliveira Taipina, M. M. F. Ferrarezi, I. V. P. Yoshida, M. do Carmo Gonçalves, *Cellulose* **2013**, *20*, 217.
[73] L. Segal, J. J. Creely, A. E. Martin, C. M. Conrad, *Text. Res. J.* **1959**, *29*, 786.
[74] A. D. French, *Cellulose* **2014**, *21*, 885.
[75] L. Xia, C. Zhang, A. Wang, Y. Wang, W. Xu, *Cellulose* **2020**, *27*, 1909.
[76] H. M. do Nascimento, A. dos Santos, V. A. Duarte, P. R. S. Bittencourt, E. Radovanovic, S. L. Fávaro, *Cellulose* **2021**, *28*, 5477.
[77] V. S. Sreenivasan, S. Somasundaram, D. Ravindran, V. Manikandan, R. Narayanasamy, *Mater. Des.* **2011**, *32*, 453.
[78] C. J. Chirayil, J. Joy, L. Mathew, M. Mozetic, J. Koetz, S. Thomas, *Ind. Crops Prod.* **2014**, *59*, 27.
[79] S. Park, J. O. Baker, M. E. Himmel, P. A. Parilla, D. K. Johnson, *Biotechnol. Biofuels* **2010**, *3*, 10.
[80] R. M. Sheltami, H. Kargarzadeh, I. Abdullah, *Sains. Malays.* **2015**, *44*, 801.
[81] W. Liu, Z. Wang, C. Hu, *Mater. Today* **2021**, *45*, 93.
[82] H. Huang, W. Wang, L. Wang, *Phys. Chem. Chem. Phys.* **2019**, *21*, 8257.
[83] F. Zhang, K. Sautter, A. M. Larsen, D. A. Findley, R. C. Davis, H. Samha, M. R. Linford, *Langmuir* **2010**, *26*, 14648.
[84] Y. Zheng, E. Cao, Y. Zhu, A. Wang, H. Hu, *J. Chem. Eng.* **2016**, *295*, 477.
[85] M. Periolatto, F. Ferrero, A. Montarsolo, R. Mossotti, *Cellulose* **2013**, *20*, 355.
[86] J E. Huheey, *J. Phys. Chem.* **1966**, *70*, 2086.
[87] J. E. Huheey, J. H. Bradbury, J. D. Leeder, J. Appl, by E. James Huheey, *J. Phys. Chem.* **1965**, *69*, 3284.
[88] S. Wang, Y. Zi, Y. S. Zhou, S. Li, F. Fan, L. Lin, Z. L. Wang, *J. Mater. Chem. A* **2016**, *4*, 3728.
[89] A. Carré, *J. Adhes. Sci. Technol.* **2007**, *21*, 961.
[90] S. Christé, J. C. G. E. Da Silva, L. P. Da Silva, *Materials* **2020**, *13*, 504.
[91] I. Kim, H. Jeon, D. Kim, J. You, D. Kim, *Nano Energy* **2018**, *53*, 975.
[92] T. Aziz, A. Ullah, H. Fan, M. I. Jamil, F. U. Khan, R. Ullah, M. Iqbal, A. Ali, B. Ullah, *J. Polym. Environ.* **2021**, *29*, 3427.
[93] Y. Liu, Q. Fu, J. Mo, Y. Lu, C. Cai, B. Luo, S. Nie, *Nano Energy* **2021**, *89*, 106369.
[94] T. Busolo, D. P. Ura, S. K. Kim, M. M. Marzec, A. Bernasik, U. Stachewicz, S. Kar-Narayan, *Nano Energy* **2019**, *57*, 500.
[95] S. Li, J. Nie, Y. Shi, X. Tao, F. Wang, J. Tian, S. Lin, X. Chen, Z. L. Wang, *Adv. Mater.* **2020**, *32*, 2001307.
[96] J. I. Brauman, J. M. Riveros, L. K. Blair, J. I. Brauman, L. K. Blair, J. Amer, *JACS* **1968**, *90*, 6561.
[97] S. Lv, X. Zhang, T. Huang, H. Yu, Q. Zhang, M. Zhu, *ACS Appl. Mater. Interfaces* **2021**, *13*, 2566.
[98] S. Parandeh, M. Kharaziha, F. Karimzadeh, *Nano Energy* **2019**, *59*, 412.
[99] R. Ccorahua, A. Cordero, C. Luyo, M. Quintana, E. Vela, *MRS Adv.* **2019**, *4*, 1315.
[100] S. Chen, J. Jiang, F. Xu, S. Gong, *Nano Energy* **2019**, *61*, 69.
[101] A. Šutka, J. Ruža, M. Järvekülg, A. Linarts, K. Mālnieks, V. Jurķāns, I. Gorņevs, J. Blūms, K. Rubenis, M. Knite, *J. Electrostat.* **2018**, *92*, 1.
[102] C. Yao, X. Yin, Y. Yu, Z. Cai, X. Wang, *Adv. Funct. Mater.* **2017**, *27*, 1700794.
[103] P. Cui, K. Parida, M. F. Lin, J. Xiong, G. Cai, P. S. Lee, *Adv. Mater. Interfaces* **2017**, *4*, 1700651.
[104] K. Shi, H. Zou, B. Sun, P. Jiang, J. He, X. Huang, *Adv. Funct. Mater.* **2020**, *30*, 1904536.
[105] H. Y. Mi, X. Jing, Z. Cai, Y. Liu, L. S. Turng, S. Gong, *Nanoscale* **2018**, *10*, 23131.
[106] H. Yang, M. Deng, Q. Tang, W. He, C. Hu, Y. Xi, R. Liu, Z. L. Wang, *Adv. Energy Mater.* **2019**, *9*, 1901149.
[107] L. Gu, L. German, T. Li, J. Li, Y. Shao, Y. Long, J. Wang, X. Wang, *ACS Appl. Mater. Interfaces* **2021**, *13*, 5133.
[108] C. Nüesch, J. A. Overberg, H. Schwameder, G. Pagenstert, A. Mündermann, *Gait Posture* **2018**, *62*, 117.
[109] V. K. Nandikolla, R. Bochen, S. Meza, A. Garcia, *J. Med. Eng.* **2017**, *2017*, 1.
[110] S. Ding, X. Ouyang, T. Liu, Z. Li, H. Yang, *IEEE Sens. J.* **2018**, *18*, 9728.
[111] S. Ding, X. Ouyang, Z. Li, H. Yang, *Sens. Actuators A Phys.* **2018**, *284*, 96.
[112] Q. Zhang, T. Jin, J. Cai, L. Xu, T. He, T. Wang, Y. Tian, L. Li, Y. Peng, C. Lee, *Adv. Sci.* **2022**, *9*, 2103694.

[113] O. Gulahmadov, M. B. Muradov, J. Kim, *ERX* **2022**, *4*, 035027.
[114] W. Zhang, Y. Zhang, G. Yang, X. Hao, X. Lv, F. Wu, J. Liu, Y. Zhang, *Nano Energy* **2021**, *82*.
[115] C. Qian, L. Li, M. Gao, H. Yang, Z. Cai, B. Chen, Z. Xiang, Z. Zhang, Y. Song, *Nano Energy* **2019**, *63*, 103885.
[116] H. Yoshihara, M. Yoshinobu, *Nord. Pulp Paper Res. J.* **2017**, *32*, 126.
[117] G. Li, T. Liu, J. Yi, H. Wang, J. Li, Y. Inoue, *IEEE Sens. J.* **2016**, *16*, 2627.
[118] Q. Chen, J. Dijken, D. Maniar, K. Loos, *Cellulose* **2023**, https://doi.org/10.1007/s10570-023-05453-9.